

Consistent representation of vapor phases in phase field crystal dynamics

Matthew J. Frick,* Emily Wilson, and Nikolas Provatas

Department of Physics, Centre for the Physics of Materials, McGill University, Montreal, QC, Canada H3A 2T8



(Received 30 June 2022; accepted 19 September 2022; published 27 February 2023)

Accurate exploration of processes involving interactions among defects, voids, and density shrinkage in rapid solidification requires the ability to simulate phase transformations over large density ranges. We begin this work by presenting a number of numerical artifacts that arise in previous attempts to model the dynamics of solid-liquid-vapor interactions using phase field crystal (PFC) models based on a single density field coupled to its mean field. We then propose a new PFC formalism for modeling solid-liquid-vapor systems that self-consistently couples two components of the density field, one varying on the usual atomic length-scales, the other on scales much greater than the atomic lattice constant. It is shown that the new formalism is free of the aforementioned artifacts exhibited by previous PFC models. We generalize this new solid-liquid-vapor PFC model to alloys and demonstrate its utility through the nucleation of voids in both a fully solid material and during solidification into a liquid.

DOI: [10.1103/PhysRevMaterials.7.023405](https://doi.org/10.1103/PhysRevMaterials.7.023405)

I. INTRODUCTION

The properties of engineering alloys are directly linked to their microstructure, which evolve in processes such as solidification, thermal and mechanical treatments, or damage. Direct imaging and *in situ* measurements of such processes is challenging and as such the vast majority of empirical knowledge on these processes comes from post mortem analysis. With the increasing availability of computational modeling the ability to predict microstructures has flourished, driven primarily by atomistic and mesoscale phase field type models. One such modeling approach is the phase field crystal formalism [1], which since its introduction has proliferated into numerous forms capable of modeling a wide range of materials phenomena. Unlike traditional phase field (PF) models a phase field crystal (PFC) model is formulated in terms of a density field that is allowed to take on periodicity in solid phases. This simple but fundamental feature makes it possible as to capture the salient physics of crystalline structure, elasticity, strain relaxation, dislocations, grain boundaries, arbitrary grain orientations, to name a few, while evolving of diffusive timescales wherein most of the relevant materials processes occur in practical materials; these effects all arise naturally and self-consistently due to the form of the basic interaction term designed into all PFC models [2]. By comparison, such mechanisms need to be built into PF models “by hand” and on a case-by-case basis depending on the mechanism of interest.

Traditionally, PFC models have been built by expansion about a fluctuating ideal gas, assumed to represent the liquid phase [3]. More recently, a number of redesigns of the PFC approach have been made to also incorporate a vapor phase both qualitatively [4] and more quantitatively [5,6]. A common feature of these models is the emergence of terms that couple the microscopic density to its mean field,

which is defined by coarse graining the microscopic density. Inclusion of the vapor phase is of great interest to the materials community, as it allows for simulation of cavitation and void formation, and the interaction of these with defects, a crucial feature for modeling rapid solidification processes emerging in materials manufacturing, and currently relegated to the very small length- and timescales via molecular dynamics. Some preliminary work has also been undertaken generalizing these models to alloy systems [7], albeit quite qualitatively.

The development of nonequilibrium microstructure is almost equally dependent on the design of the free energy as it is on the dynamical equations used to evolve the PFC density field, for pure materials, or the coupled density field and solute concentration fields in alloys. In the former, conserved Langevin-type dynamics has been used to evolve density of purely diffusive timescales set by a mobility parameter. For phenomena requiring rapid elastic relaxation to operate alongside diffusive processes, a wavelike equation of motion coined *MPFC* has been introduced [8]. In the case of alloys, the usual approach has been to evolve both the density and concentration on diffusive timescales using conserved Langevin equations of motion for both the density and concentration [9–11]. In the case of alloys, such dynamics are reasonable for solid-state processes wherein the average density between phases does not vary significantly and thus solute can be treated as a conserved quantity while the PFC density field merely keeps an accounting of crystal ordering and topological defects as discussed above. However, in rapid solidification processes such dynamics are incorrect as density changes locally and globally can be extreme. In a previous paper [12], we began the process of generating self-consistent alloy dynamics in an alloy model formulated in terms of density and concentration. This involved redefining concentration as a purely long wavelength field and exploiting the dependence of concentration and density of the elemental fields comprising the alloy.

*matthew.frick@mail.mcgill.ca

This paper begins with an examination of some recent PFC models of solid-liquid-vapor systems. We point out two recently discovered numerical artifacts that can emerge in their dynamics, which we show are linked to the fact that said models rely on certain couplings between the microscopic PFC density to its mean field via smoothing [5]. The paper then moves on to remedy these dynamical artifacts. We start by decomposing the PFC density field into two distinct field, each defined everywhere in space but one being dominant at short wavelengths and the other at long wavelengths. We reformulate some previous PFC models of pure materials in terms of this two-field representation, demonstrating that this naturally gives rise to PFC models that couple purely PFC and purely PF type term in the free energy, each of which can be manipulated separately to form new models that offer efficient and nearly separate control of the properties of periodic (solid) phase and uniform (vapor/liquid) phases. Crucially, we show that this formalism for formulating a PFC model is completely devoid of the aforementioned artifacts that emerge in past solid-liquid-vapor dynamics. The paper then moves on to adapt the above approach for modeling vapor-liquid-solid phases in binary alloys. We demonstrate that the smooth/periodic density decomposition also cures a recently discovered artifact that appears in select dynamics of PFC models that define the concentration by smoothing the component densities, namely the suppression of short wavelengths in concentration that may be relevant in specific phenomena, such as spinodal decomposition.

The remainder of this paper is organized as follows: In Sec. II we briefly review previous work that introduced vapor phase field crystal modeling and point out two numerical artifacts that emerge from these in their dynamics. In Sec. III we introduce a new approach for modeling large density changes in PFC, and a corresponding new PFC vapor-liquid-solid PFC model that addresses the aforementioned artifacts. In Sec. IV we generalize the new three-phase PFC phase model to mixtures. We conclude our work in Sec. V. A summary of models and simulation parameters is given in the Appendix.

II. PREVIOUS PFC MODELS OF VAPOR-LIQUID-SOLID SYSTEMS

The first PFC model that consistently addresses large density changes associated with vapor, liquid, and solids phases in PFC was by Kocher *et al.* [4]. This led to a consistently shaped reduced pressure-density-temperature (P-V-T) phase diagram of a pure substance and the ability to model solidification shrinkage phenomena and cavitation. Unfortunately, the model of Ref. [4] suffered from two crucial problems: (a) It exhibited unphysical vapor densities and (b) unreasonably large density gaps between the solid and liquid phases. The first problem precludes a proper description on low density phases and the second does not allow a proper description of solidification of metals in particular. Another approach for modeling the vapor phase was introduced later by Wang *et al.* [6] using real-space kernels to describe the excess energy. The approach of Ref. [6] fixed problem (b) but only at the cost of exacerbating problem (a). Follow-up work by Kocher

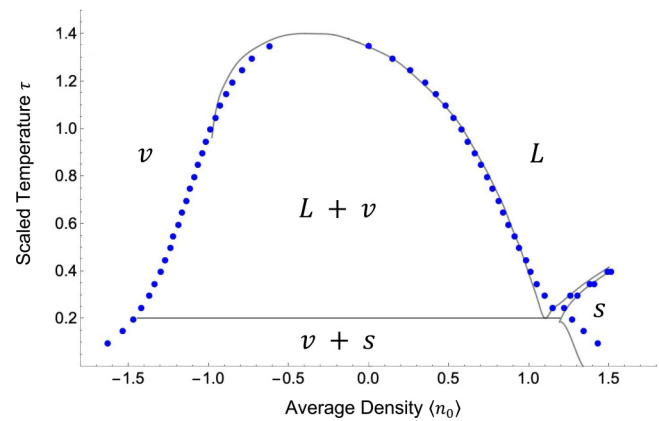


FIG. 1. Phase diagram of gold. The vertical axis is scaled temperature $\tau \equiv T/T_0$, where $T_0 = 8300$ K. The horizontal axis is density $\langle n_0 \rangle = ((\rho) - \bar{\rho})/\bar{\rho}$, where the reference density $\bar{\rho} = 5.5$ g/cm³. The solid line shows theoretical phase diagram from equation-of-state calculations of Ref. [13] while circles show the 10th-order expansion of a Van der Waals PFC free energy of Ref. [5] about $n_{mf} = 0$. See Appendix for model description and parameters.

et al. 2019 then corrected both problems (a) and (b) in the phase diagram by expanding the PFC free energy about a Van der Waals fluid [5]. Additionally, this model was shown to be robust enough to match phase diagrams rather well quantitatively, as shown in Fig. 1, which shows a fit of the parameters in the model of Ref. [5] to a phenomenological equation of state for gold taken from Ref. [13].

Further details of the process of selecting parameters for this model can be found in Ref. [14].

Despite the above advancements in the describing equilibrium properties of three-phase systems with PFC models, no attempts were made in Ref. [5] to simulate any *dynamics* of multiphase coexistence and microstructure formation in vapor-liquid-solid systems. This is noteworthy as it is in this scope of dynamical simulations that we have recently discovered that this model exhibits some limitations. Moreover, careful examination of previous three-phase models revealed that they, too, could suffer from similar artifacts in their dynamical description of microstructure. These are described in further detail below.

During attempts to study dynamical microstructure evolution in the Kocher 2019 model [5], we found a variety of odd and unphysical artifacts that can emerge. As will be discussed further below, we identified these as originating from the smoothing kernel used to construct the mean field density and certain of its couplings to the microscopic density such as to ensure that the solid-state properties do not unduly influence the liquid-vapor properties of a Van der Waals-like fluid. An example of one such dynamical artifact arises at interfaces between solid-vapor phases and is shown in Fig. 2 for three quenches in the phase diagram of Fig. 1. The root cause of this artifact is the filtering of the density into a mean field version by way of a smoothing kernel used in Ref. [5], $\tilde{\chi}(k) = e^{-k^2/(2\lambda_c^2)}$. By removing all wavelengths shorter than some cutoff this approach effectively attempts to represent an interface, which is very much like a “step function,” using a small number of long wavelength Fourier modes. Naturally, this results in a ringing effect in the mean field density, which

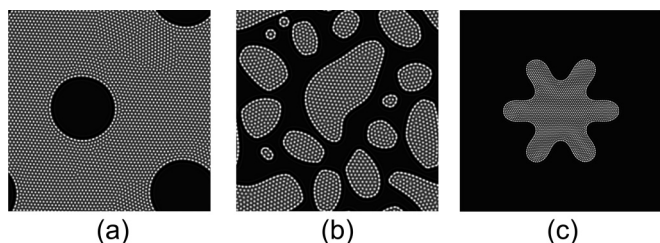


FIG. 2. Interface anomalies observed while simulating dynamics in the PFC model of Ref. [5] with the parameters used to generate Fig. 1. All results shown after 50 000 time steps. (a) Solid-vapor coexistence initiated from white noise at reduced temperature $\tau = 0.25$ and reduced average density $\langle n_0 \rangle = 1.1$. (b) Solid-vapor coexistence initiated from white noise at $\tau = 0.25$ and $\langle n_0 \rangle = 0.0$. (c) Solid-vapor coexistence initiated from a hexagonal solid seed of average density $n_s = 1.3$ in a vapor of average density $n_v = -1.3$ at $\tau = 0.25$. See Appendix for model description and parameters.

due to couplings to the crystalline amplitude result in strange and unphysical interfacial effects.

Another artifact discovered by using a filtering process to couple the mean field density to its microscopic counterpart is that it also affects the scaling domain size in select microstructure problems, most notable of which is the $t^{1/3}$ scaling of spinodal decomposition. To illustrate this, we simulated spinodal decomposition in a supercritical fluid cooled below the critical point in the phase diagram of the model in Ref. [4] (the same effect could be observed in the model of Ref. [5] that made the phase diagram in Fig. 1). The results are shown in Fig. 3. In the standard picture of spinodal decomposition the initial conditions are biased toward short wavelengths. This is either due to the addition of conserved noise, which scales approximately linearly with the wave vector, or due to numerical noise which exists on the minimum resolvable scale of the simulation. As the simulation progresses, two processes contribute to the $t^{1/3}$ domain scaling law. The first is the growth of all modes below the critical wavelength set by the domain size. The second is the passing of power from short length-scales to longer length-scales via diffusion. In effect the process begins with many small domains of overdense and underdense regions, which due to diffusion and surface energetic effects combine into larger regions. Naturally, as two or more small domains combine into a larger domain power is removed from the short wavelengths and transferred to a slightly longer wavelength. The filtering of the density using the smoothing kernel discussed above effectively removes all power from these short length-scales, thus prohibiting them from passing their power up to longer length-scales and hence removing one of the two aforementioned processes that generate the classic $t^{1/3}$ domain scaling found in spinodal decomposition. It is noted that this scaling does eventually reemerge once the average domain size is much larger than the filter cutoff wavelength.

III. IMPROVED PFC APPROACH FOR SOLID-LIQUID-VAPOUR SYSTEMS

As shown in the last section there is a need to allow for large density jumps between phases without generat-

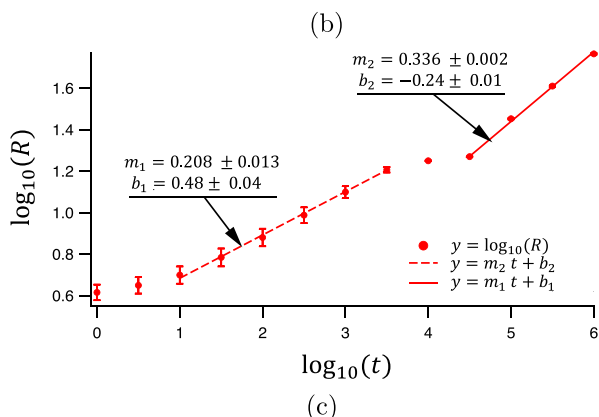
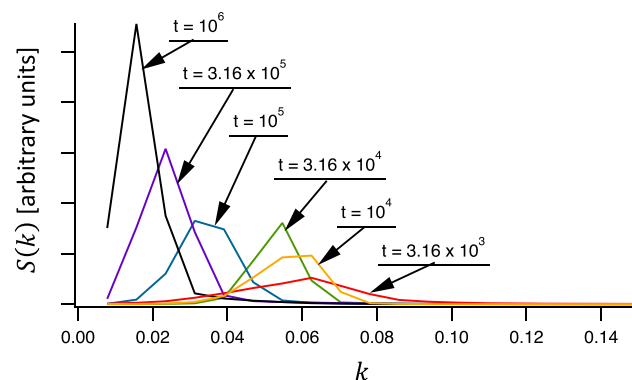
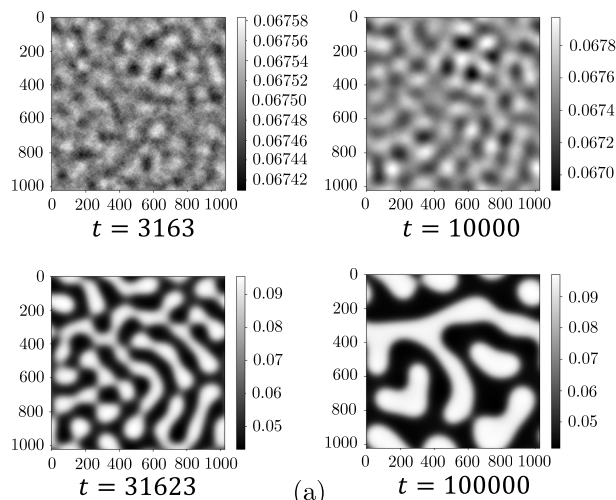


FIG. 3. Spinodal decomposition of the generic fluid phase into liquid and vapor phases. (a) Snapshots of the system as it undergoes phase separation. Time flows from left to right with the time step shown below each figure. (b) The structure factor for phase separating system, with each time shown averaged over 20 realizations. (c) Average domain size as a function of time and fits to the relatively linear portions. See Appendix for model description and parameters.

ing numerical artifacts at interfaces, both in equilibrium representations of phases as well as in dynamical microstructure evolution. To this end we introduce here an approach that takes inspiration from PFC-generated amplitude models and splits the density field n into two order parameters; a field n_0 is introduced to track density flow on long wavelengths and a field ϕ is introduced to track local crystalline ordering.

We first demonstrate the workings of these two fields by rederiving the free energy of a generic field theory used to derive most common PFC type models of a pure material. We then apply our approach to reproducing the equilibrium properties of the model of Kocher 2015 [4]. We demonstrate that by leveraging the above field decomposition, we can produce a simplified three-phase model in a way that both ensures that the vapor phase has a positive density and also exhibit reasonable liquid-solid density gaps. Crucially, we also demonstrate that the dynamical artifacts discussed in the previous section disappear from microstructure simulations using the proposed approach.

A. Decomposing the PFC density field into smooth and oscillating components

The order parameter in PFC models of a pure substance is based on the reduced microscopic density $n = (\rho - \rho_0)/\rho_0$, where ρ is the microscopically varying density and here ρ_0 is some convenient reference density of the system, for example, the liquid density at coexistence is typically cited. The ideal gas part of most PFC models is typically expanded to fourth order in n , yielding

$$\frac{F_{\text{id}}}{\rho_0 k_B T_0} = \tau \int_V dr \left\{ \frac{n^2}{2} - \frac{n^3}{6} + \frac{n^4}{12} \right\}, \quad (1)$$

where T_0 is a reference temperature around which the model is expanded and $\tau \equiv T/T_0$. We next propose a decomposition of the density n into two, at this point entirely undifferentiated and generic fields

$$n = \psi + \phi. \quad (2)$$

The fields ψ and ϕ will be endowed with properties below such that under standard coarse-graining procedures they enable easy mapping of the proposed model into a corresponding complex amplitude model [15]. For now, we merely use the binomial expansion,

$$n^m = (\psi + \phi)^m = \sum_{i=1}^m \binom{m}{i} \psi^i \phi^{m-i}, \quad (3)$$

to rewrite the free-energy density in Eq. (1) as

$$\begin{aligned} \frac{F_{\text{id}}}{\rho_0 k_B T_0} = \tau \int_V dr \left\{ \frac{\psi}{2} - \frac{\psi^3}{6} + \frac{\psi^4}{12} + \frac{\phi}{2} - \frac{\phi^3}{6} + \frac{\phi^4}{12} \right. \\ \left. + \psi\phi - \frac{1}{2}\psi\phi(\psi + \phi) \right. \\ \left. + \frac{1}{3}\psi\phi\left(\psi^2 + \frac{3}{2}\psi\phi + \phi^2\right) \right\}. \quad (4) \end{aligned}$$

It is seen that F_{id} breaks up into two decoupled ideal expressions and a set of quadratic, cubic, and quartic couplings.

Differentiation of the two fields is introduced through the excess energy. Following the standard methodology for introducing excess energies into PFC-type models, we extend Eq. (1) by generating a functional expansion in n , which on eliminating constant terms gives the standard free-energy

expansion

$$\begin{aligned} \frac{\Delta F}{\rho_0 k_B T_0} = \int_V dr \tau \left\{ \frac{n^2}{2} - \frac{n^3}{6} + \frac{n^4}{12} \right\} \\ + \frac{1}{2} \int dr \int dr' \frac{\delta^2 \tilde{F}}{\delta n(r) \delta n(r')} \delta n(r) \delta n(r'). \quad (5) \end{aligned}$$

where $\tilde{F} = (\rho_0/k_B T_0)F$, while $\Delta F = F - F_0$ with F_0 representing the free energy at the reference point of the functional expansion (ρ_0, T_0) . The second variational of the free energy is the direct two-point correlation function of the system. The functional derivatives can be applied to ψ and ϕ using the functional chain rule. This ultimately allows us to explicitly separate out direct correlation functions for ψ and ϕ , and a cross-correlation between ψ and ϕ . The algebra is straightforward and yields

$$\begin{aligned} \frac{\Delta F}{\rho_0 k_B T_0} = \tau \int_V dr \left\{ \frac{\psi^2}{2} - \frac{\psi^3}{6} + \frac{\psi^4}{12} - \frac{1}{2}\psi C_{\psi\psi} * \psi \right. \\ \left. + \frac{\phi^2}{2} - \frac{\phi^3}{6} + \frac{\phi^4}{12} - \frac{1}{2}\phi C_{\phi\phi} * \phi \right. \\ \left. + \psi\phi - \frac{1}{2}\psi\phi(\psi + \phi) \right. \\ \left. + \frac{1}{3}\psi\phi\left(\psi^2 + \frac{3}{2}\psi\phi + \phi^2\right) - \psi C_{\psi\phi} * \phi \right\}, \quad (6) \end{aligned}$$

where the notation “*” denotes convolution. The above process defines three correlation functions: $C_{\psi\psi}$ and $C_{\phi\phi}$ define self-interactions in the fields ψ , and ϕ , respectively, while $C_{\psi\phi}$ define interactions between ψ and ϕ . These correlations functions allow us to formally control interactions of the decomposed fields of our formalism at different length-scales.

Taking ψ to only represent bulk density flow within the system, a simple choice to describe its self correlation is $C_{\psi\psi} = W_n \nabla^2 \delta(r - r')$. Comparatively, taking ϕ to only represent structural ordering at the atomic scale, we may choose to define its self-correlation function in Fourier space using some function with a peak at the reciprocal lattice vector of the crystal structure in question, i.e., representing the Bragg ring as is done in XPFC models [16]. Finally, we must choose a form for the two point cross-correlation of these fields. As an example, choosing $C_{\psi\phi} = \delta(r - r')$ gives exact cancellation of the lowest-order cross-term. Such choices then result in a free energy of the form

$$\begin{aligned} \frac{\Delta F}{\rho_0 k_B T_0} = \tau \int_V dr \left\{ \frac{n_0^2}{2} - \frac{n_0^3}{6} + \frac{n_0^4}{12} + W_n |\nabla n_0|^2 \right. \\ \left. + \frac{\phi^2}{2} - \frac{\phi^3}{6} + \frac{\phi^4}{12} - \frac{1}{2}\phi C_{\phi\phi} * \phi \right. \\ \left. - \frac{1}{2}n_0\phi(n_0 + \phi) \right. \\ \left. + \frac{1}{3}n_0\phi\left(n_0^2 + \frac{3}{2}n_0\phi + \phi^2\right) \right\}, \quad (7) \end{aligned}$$

where last term in the first line was obtained by integration by parts. *It is noted that we have relabelled $\psi \rightarrow n_0$ in arriving at Eq. (7).* This is done to emphasize the connection with previous PFC and amplitude models that typically use n_0 to denote the long-wavelength density field for clarity of

form. At this point the formulation in Eq. (7) is slightly more complicated looking but functionally identical to a standard PFC model. The main difference in this two-field approach is that the small-scale structures, particularly those in crystal phases, are mainly controlled through the field ϕ , while n_0 predominantly controls long-wavelength ordering which is predominately due to changes of the bulk density of phases.

B. Adding higher-order correlations

The basic PFC model of Eq. (7) can be modified to allow for solid, liquid, and vapor phases by modifying the coefficients of some of the polynomial terms. This can be justified by invoking higher-order correlations, which contain contributions that renormalize polynomial coefficients of the basis expansion of the ideal free energy of Ref. [15]. Additionally, it is noted that cross-coupling terms between n_0 and the periodic order parameter ϕ may promote small oscillations in the n_0 field, albeit different in nature from the oscillations reported in previous PFC-amplitude papers [17]. Such effects can also be suppressed by incorporating higher-order interactions (correlations) in the excess free energy. While such interactions are not known, in what follows, we construct a phenomenology of three-point and four-point correlation functions between ϕ and n_0 that redefine the polynomial couplings of ϕ to n_0 in Eq. (7) and renormalize the polynomial coefficients in bare powers of n_0 and ϕ .

To proceed, we define a three-point correlation function between ϕ - n_0 - ϕ of the form

$$C_{\phi n_0 \phi} = \frac{6}{2}[a_3 \chi(r-r')\delta(r-r'') - \delta(r-r')\delta(r'-r'')], \quad (8)$$

where a_3 is a coupling constant. Using Eq. (8) to construct an excess free-energy term combines with the $n_0\phi^2$ term in Eq. (7) to yield

$$\begin{aligned} & -\frac{1}{2}n_0\phi^2 - \int dr' \int dr'' \frac{1}{3!}C_{\phi n_0 \phi}(r)n_0(r')\phi(r'') \\ & = -\frac{a_3}{2}\phi^2(r) \int \chi(r-r')n_0(r'). \end{aligned} \quad (9)$$

Introducing analogous forms for the other combinations of the three-point and four-point correlation functions of n_0 and ϕ , and adding these to the excess free-energy terms to Eq. (7), yields the following renormalized free energy:

$$\begin{aligned} \frac{\Delta F}{\rho_0 k_B T_0} = \tau \int_V dr \left\{ \frac{\alpha_2}{2}n_0^2 - \frac{\alpha_3}{6}n_0^3 + \frac{\alpha_4}{12}n_0^4 + W_n |\nabla n_0|^2 \right. \\ + \frac{a_2}{2}\phi^2 - \frac{a_3}{6}\phi^3 + \frac{a_4}{12}\phi^4 - \frac{1}{2}\phi C_{\phi\phi} * \phi \\ - \frac{a_3}{2}(\chi * n_0)\phi^2 + \frac{a_4}{2}(\chi * n_0)^2\phi^2 \\ \left. + \frac{a_4}{3}(\chi * n_0)\phi^3 \right\}, \end{aligned} \quad (10)$$

where $\alpha_2, \alpha_3, \alpha_4, a_2, a_3,$ and a_4 are additional constants of the two-field PFC model. It is understood that these constants may be τ dependent. The emergence of an effective smoothing on n_0 in each cross-term in Eq. (10) ensures that any potential oscillations in crystalline phases do not bleed into the bulk density field n_0 . For simplicity, we have neglected linear couplings to ϕ , as these average to zero over the lattice constant,

a feature that can be enforced to high accuracy by suitable choice of $k = 0$ mode in $C_{\phi\phi}$, which controls average density change. It is noted that such linear terms in the free energy shift the phase diagram but do not modify the overall phase behavior; as such they can be used to control quantities such as the reference pressure [4,6,12].

It is noteworthy that the model of Eq. (10) has some points of similarities with the model in Ref. [4], as well as some key differences. The latter model adds to the ‘‘standard’’ PFC model additional terms of the form $n n_{mf}^p$ where n_{mf} is a smoothing convolution of the microscopic density and $p = 2, 4$. Conversely, in Eq. (10) powers of the long-wavelength field n_0 also couple to nonlinear powers of ϕ . Furthermore, it was shown in Ref. [4] that the smooth density contribution to the interface energy is implicitly contained in the n_{mf}^2 term, as well as any $k = 0$ contribution in C_2 , the direct correlation function. Conversely, Eq. (10) allows for explicit, and easier, control of the contribution of the interface energy arising from $|\nabla n_0|^2$ term.

The model of Eq. (10) can display a variety of material phase diagrams. The procedure for making a phase diagram in the proposed PFC model follows the usual procedure outlined in Refs. [9,18]. Briefly, the total density is first expanded according to the ansatz $n_0 = \langle n_0 \rangle, \phi = \sum_j \eta_j e^{i\vec{G}_j \cdot \vec{r}} + c.c.$, where η_j are the [constant] amplitudes of the density wave with reciprocal wave vector \vec{G}_j and the index j runs over wave vectors of the Brillouin zone for the crystal structure being probed; here we retain only \vec{G}_j in the first Brillouin zone. This expansion is substituted into the integrand of Eq. (10) and the result is integrated over the unit cell of the crystal. The result is a mean field free-energy density of the form $\mathcal{F}(n_0, \{\eta_j\})$. This is minimized with respect to the amplitudes η_j^* (since, by construction, the average of ϕ is zero) and the result, $\mathcal{F}(n_0, \{\eta_j^*(n_0)\})$, is analyzed by a common tangent construction to find coexistence values of n_0 , and the corresponding chemical potential. When the model constants are set such that $\alpha_2 = a_2, \alpha_3 = a_3, \alpha_4 = a_4$, and each constant is near unity, the model is a two-field representation of the ‘‘standard’’ PFC model [3] and yields a similar phase diagram. However, when temperature dependence is introduced to the α_m constants we recover the same vapor-liquid-solid phase diagram of Ref. [4] as shown in Fig. 4.

C. Dynamics

As a density field n is assumed, in the diffusive time limits, to follow the usual conserved dynamics. Since $n = \psi + \phi$, this gives

$$\frac{\partial n}{\partial t} = M \nabla^2 \frac{\delta F}{\delta n} = M \nabla^2 \frac{\delta F}{\delta n_0} + M \nabla^2 \frac{\delta F}{\delta \phi}. \quad (11)$$

The first term on the right-hand side of Eq. (11) can be identified as a gradient in the flux that governs density changes on long wavelengths, while the second term represent a gradient flux that governs density changes on short wavelengths. Making the assumption that density flow on long and short wavelengths is separately conserved allows us to use the procedure used in multiscale analysis [18,19] to decouple the

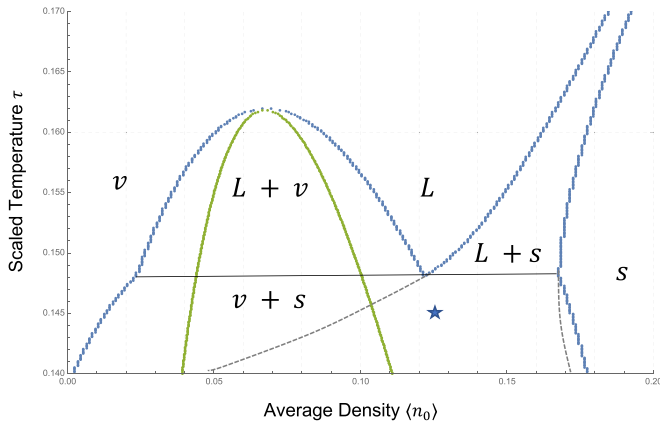


FIG. 4. Replication of the phase diagram for the three phase system in Ref. [4] using the model in Eq. (10). Metastable solidus and liquidus lines are shown by the dashed lines. Average density and temperature values for the simulation shown in Fig. 5 is marked by the star in the phase diagram. See Appendix for model description and parameters.

dynamics of n_0 and ϕ according to

$$\frac{\partial n_0}{\partial t} = M \nabla^2 \frac{\delta F}{\delta n_0}, \quad \frac{\partial \phi}{\partial t} = M \nabla^2 \frac{\delta F}{\delta \phi}. \quad (12)$$

It is noted that Eq. (12) satisfies the overall density conservation since the sum of any two conserved quantities must also be conserved. These dynamics are analogous to previous dynamics that decouple the evolution of the smooth density from that of complex order parameters in amplitude equations derived from PFC models in the sense that they explicitly separate the evolution of length-scales describing mass density flow and crystalline ordering [15,20,21]. Indeed, by expressing powers of the ϕ terms in the Eq. (10) in terms of corresponding powers of complex amplitude that encode for a particular crystal structure and orientation, it is relatively simple to complete the coarse graining of the Eq. (12) into a complex amplitude model.

It is recalled that it was certain numerical artifacts in the dynamics in previous vapor-liquid-solid PFC models that prompted us to reformulate a vapor-liquid-solid PFC model in terms of two independent but coupled fields. As a first test of the dynamics in a vapor-liquid-solid system driven by the model in Eq. (10), we reproduce the seaweed dendrite structure of Kocher 2015 [4]. We use the parameters for the phase diagram in Fig. 4. We perform a quench to a reduced temperature of $\tau = 0.145$ and system average density $n_0 = 0.125$ as shown by the star on the phase diagram in Fig. 4. The resulting microstructure is shown in Fig. 5. The initial solid seed grows, eventually nucleates a vapor phase at its boundary and then undergoes competitive growth of the two phase system. It is noted that in contrast to Fig. 2, here interfaces between phases show a smooth and gradual transition on the scale of a few lattice constants.

As a second consistency check on the dynamics driven by the free energy in Eq. (10), we also simulated sinodal decomposition of a liquid analogous to that in Fig. 3. For this simulation, we added conserved Gaussian noise to Eqs. (12). The results are shown in Fig. 6. The data confirm proper $t^{1/3}$

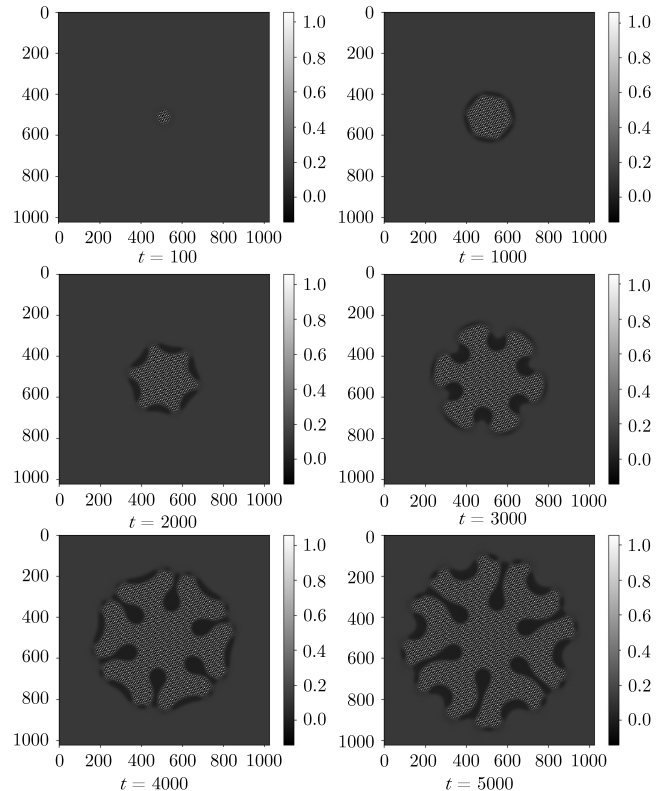


FIG. 5. Simulation of the three phase dendrite analogous to that shown Ref [4] using the model proposed in this work. Time flows from left to right and top to bottom with the time steps shown below each figure. The quench temperature is shown in Fig. 4. See Appendix for model description and parameters.

scaling of the inverse peak position of the power spectrum of the domain sizes. After an initial transient time the system settles into the well-established behavior, in contrast to the anomalous scaling regime exhibited in Fig. 3. The proper scaling also emerges approximately a decade earlier when compared to the filtered model.

It is noted that in both test cases examined above, as well as in the simulations to follow in the following sections, the dynamics of the models derived in this work are performed using the semi-implicit Fourier method due to the important role played by the filtering convolutions in maintaining the initial assumptions of the model.

D. Quantitative improvements to the formalism

This subsection generalizes the approach leading to the two-field PFC model Eq. (10) in order to generate a more realistic three-phase PFC model for a pure material using the approach developed in the previous subsection. We begin by acknowledging a flaw of using the Van der Waals (VdW) formalism to fit both the free energy of disordered and solid phases; namely VdW theory is designed around low densities and high temperatures. In the high-temperature or low-density approximation, interactions are assumed to emerge from the excluded volume of a particle, which is equal to the minimal enclosing sphere containing exactly two hard spheres. By

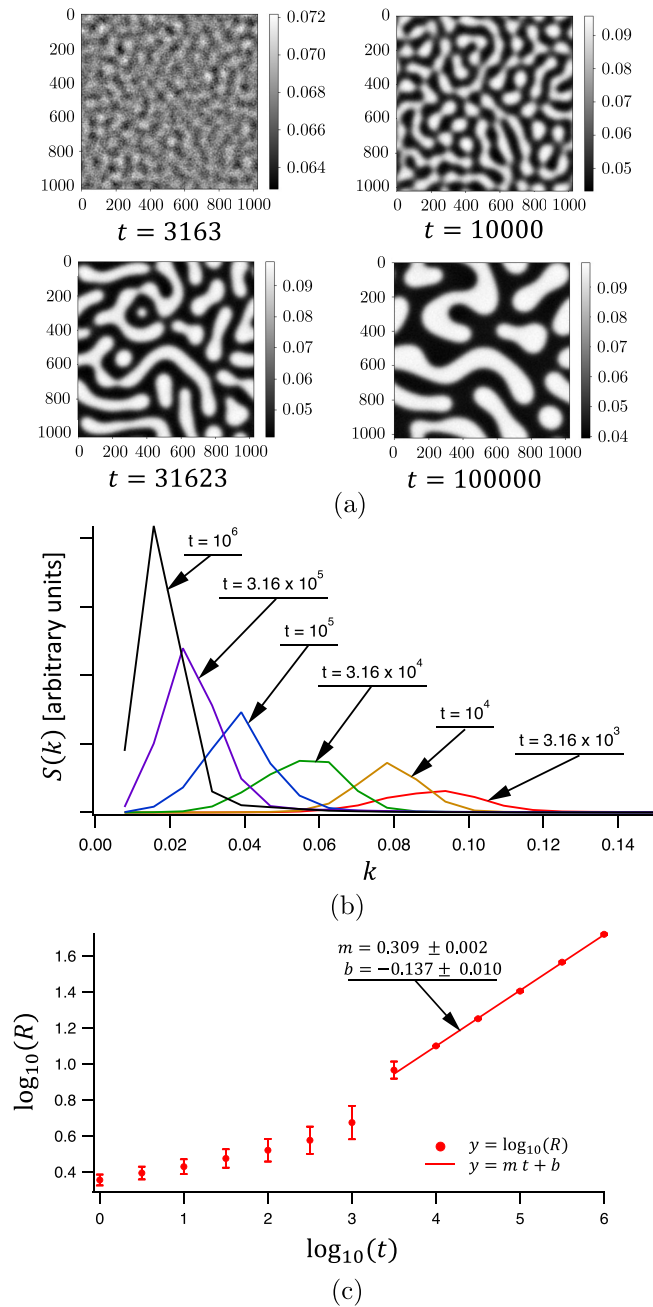


FIG. 6. Spinodal decomposition of a fluid phase into liquid-vapor phases corresponding to the phase diagram in Fig. 4. (a) Example snapshots of phase separation at different times. (b) Structure factor for the phase-separating system averaged over 20 realizations. (c) Average domain size as a function of time and fit to extract scaling exponent. See Appendix for model description and parameters.

comparison, at low temperatures or high density, interactions require some form of attractive, temperature-dependent interaction, which are missing from VdW theory. Thus, describing a high-density closed packed solid with a VdW model will inevitably trigger an infinite energy through the excluded volume mechanism. Moreover, a VdW description of a solid at low-enough temperatures will lead to free-energy energy

curvatures near equilibrium (i.e., driving force) that becomes numerically intractable.

We propose to solve the above problem by modifying the n_0 expansion of free energy in Eq. (10) to take on a Van der Waals form at low average densities (i.e., in uniform phases) and to transition to its usual ideal gas form at high densities, whereupon the ϕ part of the free energy will be active to control the properties of solid phases. To achieve this we must add an energetic barrier contribution to the free energy around a density $n_0 = n_c$ that lies somewhere between two the liquid and vapor phases. The precise mathematical form of the free energy barrier is not critical; its true form can, in theory, be considered as arising from an infinite series in n_0 arising in from the higher-order excess free energy terms, which would in principle lead to a free energy barrier emerging in the n_0 form of the free energy. We choose here to represent this barrier through the simple form $\sim e^{(n_0 - n_c)^2}$, which leads to a revised model of the form

$$\begin{aligned} \frac{\Delta F}{\rho_0 k_B T_0} = \tau \int_V dr \left\{ \frac{n_0^2}{2} - \frac{n_0^3}{6} + \frac{n_0^4}{12} + \frac{a}{\sqrt{\tau^2 + \tau_*^2}} e^{-(n_0 - n_c)^2} \right. \\ + W_n |\nabla n_0|^2 - \frac{1}{2} \phi C_{\phi\phi} * \phi \\ + \frac{a_2}{2} \phi^2 - \frac{a_3}{6} \phi^3 + \frac{a_4}{12} \phi^4 \\ - \frac{a_3}{2} (\chi * n_0) \phi^2 + \frac{a_4}{2} (\chi * n_0)^2 \phi^2 \\ \left. + \frac{a_4}{3} (\chi * n_0) \phi^3 \right\}. \end{aligned} \quad (13)$$

Here a is another constant, n_c is the critical density of the liquid-vapor spinodal and $\tau_* \equiv T_*/T_0$, where T_0 is the a reference temperature for the whole model and T_* is a cutoff temperature that ensures that the attractive interaction remains finite in the low-temperature limit. This form recovers the attractive component of the Van der Waals model near the critical fluid density n_c , which can be seen by expanding the exponential about the critical density $n_0 = n_c$ in the limit where temperature $T \gg T_*$ gives $e^{-(n_0 - n_c)^2} / (a\sqrt{T^2 + T_*^2}) \approx -\frac{a}{T} (n_0 - n_c)^2$. Higher-order contributions capture the behavior of the repulsive term at larger densities. Crucially, because of the rapid decay of the Gaussian function at large n_0 prohibits the Van der Waals-type behavior Eq. (13) from imposing itself at high densities.

A typical phase diagram for the model in Eq. (13) is shown in Fig. 7. We verified the consistency of this phase diagram dynamically by conducting conserved Langevin dynamics to confirm the bulk densities follow the tie lines of the phase diagram at different temperatures and for different phase combinations shown. Dynamical simulations of microstructure evolution were conducted to ensure that no unphysical interface artifacts emerge of the type found in previous three-phase PFC models, discussed in the previous section. Figure 8 shows snapshots in time of these simulations. Figure 8(a) shows the process of phase separation by spinodal decomposition, revealing the typical coarsening of domains sizes. Figure 8(b) shows a solid seed growing into a slightly overdense liquid, ultimately reaching equilibrium with corresponding solid/liquid phase fractions predicted by the phase diagram. Figure 8(c)

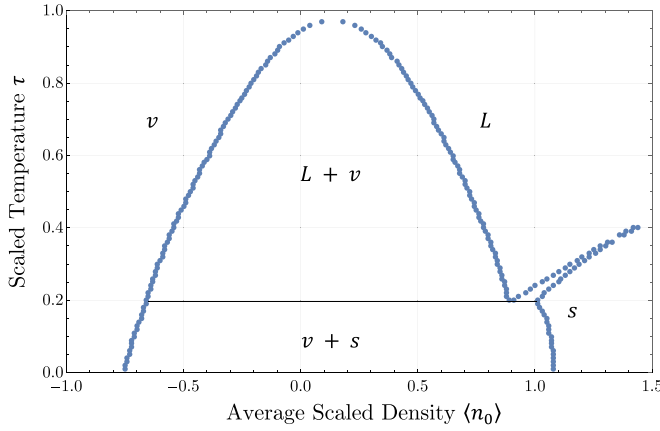


FIG. 7. An example phase diagram for the more realistic pure material using this simplified model. See the Appendix for model parameters.

shows a circular solid seed growing into a metastable liquid; as time progresses vapor pockets nucleate within the depletion layer surrounding the growing crystal, and accretion layers around vapor pockets cause the solid to quickly surround and entrap them, significantly slowing their growth.

IV. GENERALIZATION TO MULTI-PHASE MIXTURES

This section generalizes the approach of Sec. III to PFC modeling of vapor-liquid-solid phases in binary mixtures. The basis of this will again be to decompose the PFC total density order parameter into two smooth components and one oscillating component and then derive a phenomenology incorporating vapor, liquid, and solid phases in terms of these two fields and concentration. We begin by first briefly reviewing the traditional two-phase (solid-liquid) XPFC model of a binary alloy. We then introduce the three-field decomposition of the density into the alloy formalism. Following that, we modify the alloy model to contain a van der Waals contribution to enable a vapor-liquid decomposition of the uniform phase. Finally, alloy dynamics are defined in terms of the three density fields and concentration.

A. Traditional three-phase PFC alloy model

Standard approach for deriving an XPFC model for modeling crystallization of a liquid in binary alloy begins with the following free energy [9]:

$$\mathcal{F}[\rho_A, \rho_B] = k_B T \sum_i \int dr \left\{ \rho_i(r) \ln \left[\frac{\rho_i(r)}{\rho_i^0} \right] - (1 - \mu_i^*) \Delta \rho_i(r) - \frac{1}{2} \sum_{i,j} \Delta \rho_i(r) C_{ij}^{(2)}(r, r') * \Delta \rho_j(r') \right\}, \quad (14)$$

where ρ_i is the density of species $i = A, B$ and $\Delta \rho_i = \rho_i - \rho_i^0$, where ρ_i^0 is a reference density of component i around which the free energy is expanded. Here $\mu_i^* = \mu_i^0/k_B T$, where μ_i^0 is the chemical potential of component i at the reference density ρ_i^0 . Interactions are contained in the

$C_{ij}^{(2)}$, which represent the usual two-point direct correlation functions. In the context of classical density-functional theory, $k_B T C_{ij}^{(2)}(\mathbf{r}, \mathbf{r}') = \delta F / \delta \rho_i(\mathbf{r}) \delta \rho_j(\mathbf{r}')$ about the reference densities ρ_A^0 and ρ_B^0 . In PFC modeling, these are typically constructed to stabilize crystal structures [9,18,22].

In metal alloys, it is usually convenient to work with the total density $\rho = \rho_A + \rho_B$ and the local concentration $c = \rho_B / (\rho_A + \rho_B)$. These quantities allow our system to be described in terms of metallurgical parameters and conditions. In order to work with an expanded theory around reference densities, we transform to variables n and c once more according to

$$n = (\rho_A + \rho_B) / \rho_0 - 1 \\ \Delta c = \rho_B / (\rho_A + \rho_B) - c_0, \quad (15)$$

where $\rho_0 \equiv \rho_A^0 + \rho_B^0$ and $c_0 = \rho_B^0 / (\rho_A^0 + \rho_B^0)$ is the concentration at the reference densities. It is further assumed that the concentration field c (or Δc) is uniform on length-scales larger than the lattice constant of the crystal, an assumption that is fair only for substitutional alloys but not interstitial alloys. We will be considering substitutional alloys here.

Under the above assumptions on n and Δc , the free-energy functional in Eq. (14) simplifies to

$$\Delta F = \rho_0 k_B T \int dr \left\{ \frac{n^2}{2} - \frac{n^3}{6} + \frac{n^4}{12} + (n+1) S_{\text{mix}}(n, c) - (n+1)[(1-c)\mu_A^* + c\mu_B^*] - \frac{1}{2} n C_{nn}(\mathbf{r}, \mathbf{r}') * n - \frac{1}{2} \Delta c C_{cc}(\mathbf{r}, \mathbf{r}') * \Delta c \right\}. \quad (16)$$

In arriving at Eq. (16), the logarithmic terms from ideal gas free energy are expanded according to $(n+1) \ln(n+1) \approx n^2/2 - n^3/6 + n^4/12$. The other expressions in Eq. (16) are as follows: $\mu_A^* = 1 - \mu_A^0/k_B T$ and $\mu_B^* = 1 - \mu_B^0/k_B T$, with μ_i^0 ($i = A, B$) being the equilibrium chemical potential of component i at the reference density, and

$$S_{\text{mix}} = c \ln \left(\frac{c}{c_0} \right) + (1-c) \ln \left(\frac{1-c}{1-c_0} \right) \quad (17)$$

is the entropy of mixing, where c_0 is the reference-state concentration. These reference chemical potentials are given by model parameters that are assumed constant and thus are themselves constant. As in the pure material, their primary contribution would be to quantify thermodynamic values at the reference density. These chemical potentials are typically set to $\mu_A^* = \mu_B^*$ such that the second line of Eq. (16) reduces to $-n$; this corresponds to a liquid-state equilibrium where $c = \frac{1}{2}$. Here $C_{nn} = \delta \bar{F} / \delta n(\mathbf{r}) \delta n(\mathbf{r}')$ and $C_{cc} = \delta \bar{F} / \delta c(\mathbf{r}) \delta c(\mathbf{r}')$ are effective direct correlation function for total density and concentration, respectively [in the notation of Eq. (5)]. For simplicity, cross-correlation terms between n and Δc are ignored in what follows, although this is not necessary. Both C_{nn} and C_{cc} are formally given in terms of the species correlations $C_{ij}^{(2)}$. However, they typically need to be modified to yield practical alloy systems. In the case of smooth c field, only the $k \rightarrow 0$ limit of C_{cc} is retained, giving $C_{cc} \sim \nabla^2 \delta(\mathbf{r} - \mathbf{r}')$ [23]. Meanwhile, to model eutectic alloys a convenient choice

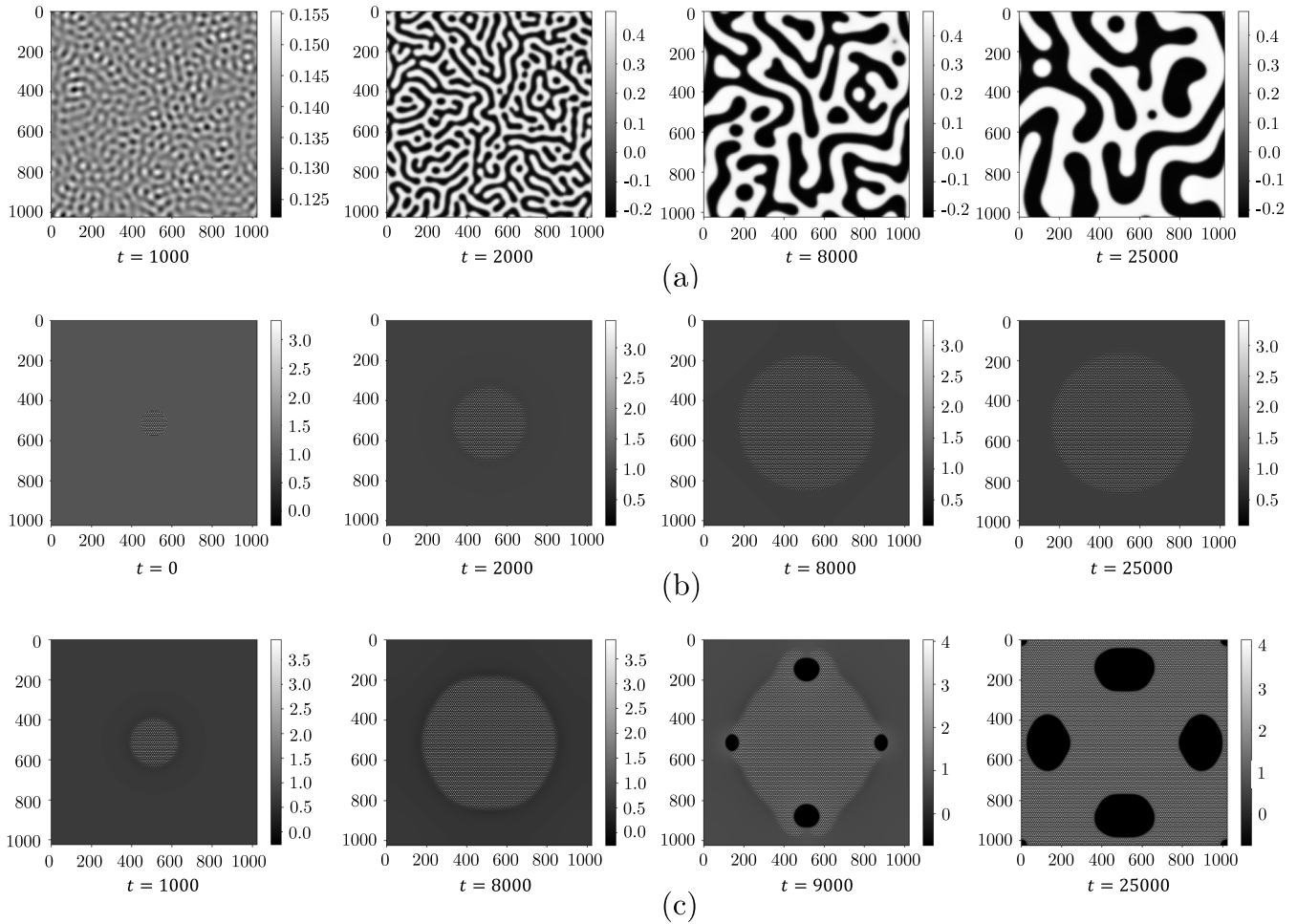


FIG. 8. Simulations of phase growth and coexistence using the model of Eq. (13), whose phase diagram is given by Fig. 7. In each case time flows from left to right, where the numerical time is shown below the figure. (a) Liquid-vapor phase separation at $\tau = 0.8$ and $n_0 = 0.14$. (b) Solid seed growing toward solid-liquid coexistence at $\tau = 0.21$ and $n_0 = 0.93$. (c) Seeded circular solid seed growing into a metastable liquid at $\tau = 0.12$ and $n_0 = 0.7$, ultimately evolving toward solid-vapor coexistence. See Appendix for model description and parameters.

for C_{mn} is given by [9,10,22]

$$C_{mn} = X_A(c)C_{AA}(r, r') + X_B(c)C_{BB}(r, r'), \quad (18)$$

where (X_A, X_B) are interpolation functions defined by

$$X_A(c) = 1 - 3c^2 + 2c^3, \quad X_B(c) = 3c^2 + 2c^3, \quad (19)$$

which we shall continue to use in this work.

A recent PFC work [12] imposed the smoothness condition on the concentration by explicitly writing it $c = \chi * \rho_B / \chi * (\rho_A + \rho_B)$. This was an important step for deriving alloy dynamics directly in terms of individual species densities ρ_A and ρ_B by applying the functional chain rule to $\Delta F[n, c]$ [via Eq. (15)] to derive $\delta \Delta F / \delta \rho_A$ and $\delta \Delta F / \delta \rho_B$. This approach assures conserved dynamics in each species density, which is an important step toward modeling large density jumps between phases. However, this smoothing ansatz on c may also produces some artifacts, such as in the dynamics of spinodal decomposition, which involves the transference of information from short to long wavelengths (it does not, however, preclude the study of other solidification and grain growth problems.) The next section will reformulate the model of

Eq. (16) to expand its scope to three-phase alloys, which will also turn out to remedy this artifact.

B. Decomposing the alloy density into smooth and oscillating components: Multiphase alloys

To go beyond the three-phase (two solids and liquid) model of Eq. (16), we will take a similar approach as we did for pure materials. We begin by decomposing the density n explicitly into two fields, one dominated by low- k modes the other by high- k modes. In analogy with the section on pure materials we thus decompose the PFC density field for alloys into a smooth and rapidly oscillating part, according to

$$n = n_0 + \phi, \quad (20)$$

where now n_0 itself is further assumed to be the sum of two contributions,

$$n_0 = n_0^A + n_0^B. \quad (21)$$

In terms of these definition, the c field can now be naturally expressed in terms the variables n_0^A and n_0^B as

$$\Delta c = \frac{n_0^B}{n_0^A + n_0^B + 1}. \quad (22)$$

PFC alloys can now be expressed in terms of the three fields (n_0, c, ϕ) and implicitly in terms of the four fields (n_0^A, n_0^B, c, ϕ) .

To proceed further, we follow the same procedure as in the single-component case, namely substitute Eq. (20) into Eq. (16) and use the functional chain rule to derive $C_{\phi\phi}$ and $C_{n_0 n_0}$ from C_{nn} . In the resulting expansion, the bulk components of Eq. (16) that depend on c , as well as C_{cc} remain the same, except that now c is assumed follow Eq. (22), which will become relevant for dynamics. As in the pure material, we take $C_{n_0 n_0} = W_n \nabla^2 \delta(\mathbf{r} - \mathbf{r}')$, while now $C_{\phi\phi}$ follows Eq. (18). Finally, to include a vapor phase into the model, we also add to Eq. (16) the higher-order three-point and four-point correlation functions defined in Eq. (8), thus making the reformulated alloy PFC model capable of supporting solid, liquid, and vapor phases. We will not show the straightforward but tedious algebraic steps here as they are very similar to those in the previous section. The result is a model of the form

$$\begin{aligned} \frac{\Delta F}{\rho_0 k_B T_0} = \tau \int_V d\mathbf{r} \left\{ \frac{\alpha_2}{2} n_0^2 - \frac{\alpha_3}{6} n_0^3 + \frac{\alpha_4}{12} n_0^4 + W_n |\nabla n_0|^2 \right. \\ + \frac{a_2}{2} \phi^2 - \frac{a_3}{6} \phi^3 + \frac{a_4}{12} \phi^4 - \frac{1}{2} \phi C_{\phi\phi} * \phi \\ + w(n_0 + 1) \left[c \ln \left(\frac{c}{c_0} \right) + (1 - c) \ln \left(\frac{1-c}{1-c_0} \right) \right] \\ - \frac{1}{2} c C_{cc} * c - \frac{a_3}{2} (\chi * n_0) \phi^2 \\ \left. + \frac{a_4}{2} (\chi * n_0)^2 \phi^2 + \frac{a_4}{3} (\chi * n_0) \phi^3 \right\}. \quad (23) \end{aligned}$$

It is recalled that the reasons for including higher-order correlations are twofold. The first is to allow us to generalize the n_0 and ϕ expansions. The second is to further suppress any small oscillations in n_0 and c that arise due to coupling of the smooth fields to powers of ϕ . For completeness, we thus also modify the interpolation functions in c for C_{nn} to the form

$$\begin{aligned} X_A &= 1 - 3(\chi * c)^2 + 2(\chi * c)^3, \\ X_B &= 3(\chi * c)^2 - 2(\chi * c)^3. \end{aligned} \quad (24)$$

Equation (23) is a minimal model for a PFC alloy with three phases, solid, liquid, and vapor, with the latter phase being controlled via the sets of constants $\{\alpha_i, a_i\}$.

C. Quantitative improvements to the alloy model

Equation (23) provides a generic model liquid-vapor coexistence in alloys with limited control of the phase diagram. As in the case of a single component, more quantitative control of the liquid-vapor properties of the model can be achieved by selectively modifying only the n_0 part of the free-energy expansion to include a phenomenological addition that includes an energy barrier at densities in between the liquid and vapor phases. To learn how to do so, we first digress to examine the specific form that a VdW interaction takes in alloys.

A simple van der Waals contribution to the alloy free energy can be motivated by the partition function of a multicomponent Van der Waals fluid, as used previously in the nuclear physics literature [24]. The hard sphere excluded volume portion of this partition function remains unchanged when porting over to our condensed matter applications in crystallization; only the attractive potential will change. The partition function for a K -component fluid is given by

$$Z = \prod_{q=1}^K \frac{1}{N_q!} \left[\frac{e^{-\frac{\phi_q}{k_B T}} (V - \sum_{p=1}^K N_p b_{pq})}{\Lambda_q^d} \right]^{N_q}, \quad (25)$$

where N_q is the number of particles of type q ; b_{pq} is the excluded volume of a p - q collision, given by half the minimal volume d -sphere that can fully enclose two particles, one of type p and one of type q ; Λ_q is the deBroglie wavelength of a particle of type q ; and d is the number of dimensions. Here we posit that interaction energy, ϕ_q , is given by

$$\phi_q = \sum_{p=q}^K \left(-2 a_{pq} \frac{N_p}{V} \right), \quad (26)$$

where a_{pq} is the averaged attraction strength between particles of type p and q . In what follows, we will limit ourselves, in this work, to two components N_A and N_B . From Eq. (25) is derived a free energy that contains a purely Van der Waals component, $S_{\text{vdW}}(N_A, N_B)$. In the continuum limit of a fluid, $N_A \rightarrow n_A^0(\mathbf{x}, t)$ and $N_B \rightarrow n_B^0(\mathbf{x}, t)$, where \mathbf{x} denotes position of a local volume element in the system and t is time. Correspondingly, $S_{\text{vdW}}(N_A, N_B) \rightarrow S_{\text{vdW}}(n_A^0, n_B^0)$. In the alloy variables defined in Eq. (21) and Eq. (22), this becomes

$$\begin{aligned} S_{\text{vdW}} &= (1 - c) \ln \left\{ \frac{1 - (1 - c_0)b_{AA} - c_0 b_{BA}}{1 - (n_0 + 1)[(1 - c)b_{AA} + c b_{BA}]} \right\} \\ &+ c \ln \left\{ \frac{1 - (1 - c_0)b_{AB} - c_0 b_{BB}}{1 - (n_0 + 1)[(1 - c)b_{AB} + c b_{BB}]} \right\}, \quad (27) \end{aligned}$$

where here μ_A^* and μ_B^* are given by

$$\begin{aligned} \mu_A^* &= 1 - \frac{\mu_A}{k_B T} \\ &- (1 - c_0) \left[\frac{b_{AA}}{1 - (1 - c_0)b_{AA} - c_0 b_{BA}} - 2 \frac{a_{AA}}{k_B T} \right] \\ &- c_0 \left[\frac{b_{AB}}{1 - (1 - c_0)b_{AB} - c_0 b_{BB}} - \frac{a_{AB} + a_{BA}}{k_B T} \right] \quad (28) \end{aligned}$$

and

$$\begin{aligned} \mu_B^* &= 1 - \frac{\mu_B}{k_B T} \\ &- (1 - c_0) \left[\frac{b_{BA}}{1 - (1 - c_0)b_{AA} - c_0 b_{BA}} - \frac{a_{AB} + a_{BA}}{k_B T} \right] \\ &- c_0 \left[\frac{b_{BB}}{1 - (1 - c_0)b_{AB} - c_0 b_{BB}} - 2 \frac{a_{BB}}{k_B T} \right]. \quad (29) \end{aligned}$$

With Eq. (27) as a reference, we modify the n_0 part of Eq. (23) to include an energy barrier in the range of n_0 between the liquid and vapor phases. This can, in principle, be constructed by constructing an infinite series in n_0 that arises from higher order, multipoint, correlation functions that

couple c to n_0 . One phenomenological modification to the model in Eq. (23) that achieves this goal is

$$\begin{aligned} \frac{\Delta F}{\rho_0 k_B T_0} = & \tau \int_V dr \left\{ \frac{n_0^2}{2} - \frac{n_0^3}{6} + \frac{n_0^4}{12} + W_n |\nabla n_0|^2 \right. \\ & + \left[\frac{(1-c)^2 a_{AA} + 2c(1-c)a_{AB} + c^2 a_{BB}}{\sqrt{\tau^2 + \tau_*^2}} \right] \\ & \times e^{-(n_0 - n_c)^2} + \frac{a_2}{2} \phi^2 - \frac{a_3}{6} \phi^3 + \frac{a_4}{12} \phi^4 \\ & - \frac{1}{2} \phi C_{\phi\phi} * \phi + w(n_0 + 1) \left[c \ln \left(\frac{c}{c_0} \right) \right. \\ & + (1-c) \ln \left(\frac{1-c}{1-c_0} \right) \left. \right] - \frac{1}{2} c C_{cc} * c \\ & - \frac{a_3}{2} (\chi * n_0) \phi^2 + \frac{a_4}{2} (\chi * n_0)^2 \phi^2 \\ & \left. + \frac{a_4}{3} (\chi * n_0) \phi^3 \right\}. \end{aligned} \quad (30)$$

As with the pure material, this free energy captures the key feature of the Van der Waals alloy—a spinodal between the liquid and solid. It is noteworthy, however, that in the case of the alloy, the magnitude of the energy well near the spinodal is now c dependent. It is also noted that the above alloy model does not drive the vapor toward negative densities.

We constructed several phase diagram for a four-phase alloy in Eq. (30). Making a phase diagram for an alloy with a vapor phase is analogous to a ternary phase diagram. The process is described in detail in Refs. [12,25] and is thus only reviewed here to keep the length of this work tractable. We begin by substituting a mode expansion of the crystal phase of interest into the free energy density of the ΔF functional and then integrating it over the unit cell of the crystal. This will then give a mean-field-type free energy of the form $\Delta \bar{F}(\{\eta_j\}, n_0, c)$, where $\{\eta_j\}$ are the set of amplitudes of the oscillating field ϕ and where here n_0 and c represent bulk averages in a phase (i.e., $\langle n_0 \rangle$ and $\langle c \rangle$). As with the case of a pure material, $\Delta \bar{F}$ is minimized with respect to each η_j , after which the mean-field free energy becomes $\mathcal{F}(c, n_0) \equiv \Delta \bar{F}(\{\eta_j^*(c, n_0)\}, n_0, c)$ where η_j^* denote the minimized amplitudes of the mode expansion of ϕ . From here, the equilibrium states of \mathcal{F} are constructed using a *common plane* construction, whereby the convex hull of \mathcal{F} is found using a numerical procedure (e.g., using the convex hull functionality of Mathematica). From the convex hull the tie line passing through any (n_0, c) pair is found. The ends of this tie line define the equilibrium states and their corresponding equilibrium bulk values of n_0 and c .

A number of constant temperature phase diagrams for a binary alloy corresponding to the model free energy in Eq. (30) were constructed. Figure 9 shows two $(\langle c \rangle, \langle n_0 \rangle)$ phase diagrams for a eutectic alloy containing a vapor phase. These reveal the robustness of our new PFC formalism to model two and three phase coexistence between one or two solids phases, liquid and vapor.

We also constructed a phase diagram following the approach of Ref. [12] to construct a phase diagram under the constraint of constant pressure, an important case for modeling mechanisms relevant to experiments, which are typically

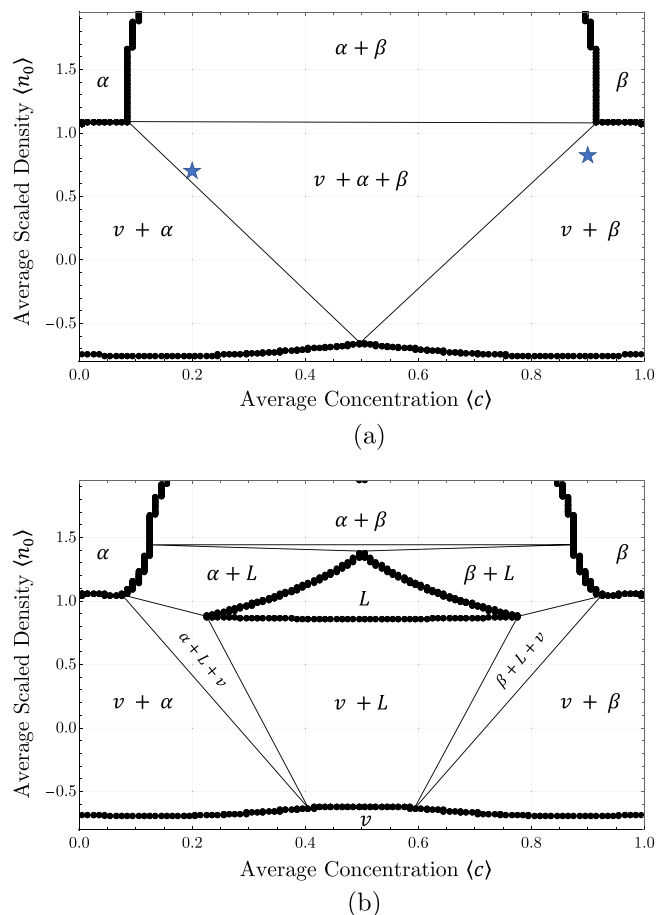


FIG. 9. Selection of isothermal phase diagrams for a eutectic binary alloy capable of supporting both liquid and vapor fluidic phases. Phase diagrams are at scaled temperature of (a) $\tau = 0.025$, and (b) $\tau = 0.15$. The stars in (a) denote the two and three phase coexistence simulated in Figs. 11 and 12, respectively. See Appendix for model description and parameters.

conducted in an open, constant-pressure environment. Figure 10 shows a constant pressure phase diagram for the same eutectic alloy system as in Figure 9.

D. Three-phase alloy dynamics

As discussed in the recent work of Frick *et al.* [12], the truly conserved dynamical variables of alloy systems are the constituent densities n_A^0 and n_B^0 ; concentration is not strictly conserved in the presence of a changing total density. The approach of that work was to exploit the fact that c is formally a function of the two species densities n_A and n_B (through a smoothing operation). Applying the functional chain rule on the free-energy functional of the form $\Delta F[n(n_A^A, n_B^B), c[n_A^A, n_B^B]]$ made it possible to derive dynamics for each dimensionless density field n_A and n_B . Applying the methodology of Ref. [12] to Eq. (30), using the relations in Eqs. (20)–(22), we arrive at the following dynamical equations for n_A^0 , n_B^0 , and ϕ :

$$\frac{\partial n_A^0}{\partial t} = M_A \nabla^2 \left[\frac{\delta F}{\delta n_0} - \left(\frac{c}{n_0 + 1} \right) \frac{\delta F}{\delta c} \right],$$

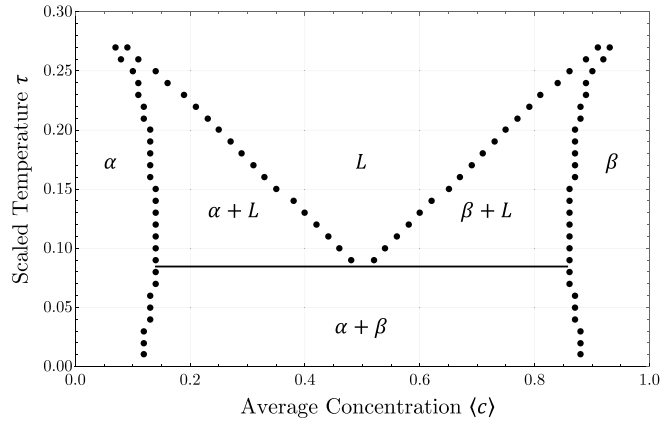


FIG. 10. Constant pressure cut of the same phase diagram as in Fig. 9 at scaled pressure $\mathcal{P} = 0.05$. See Appendix for model description and parameters.

$$\begin{aligned} \frac{\partial n_B^0}{\partial t} &= M_B \nabla^2 \left[\frac{\delta F}{\delta n_0} + \left(\frac{1-c}{n_0+1} \right) \frac{\delta F}{\delta c} \right], \\ \frac{\partial \phi}{\partial t} &= M_\phi \nabla^2 \frac{\delta F}{\delta \phi}. \end{aligned} \quad (31)$$

The key simplification in Eq. (31) compared to the formulation in Ref. [12] arises from the fact that since this model is directly formulated in terms of the fields n_0 and c , which are smooth by construction, there is no longer

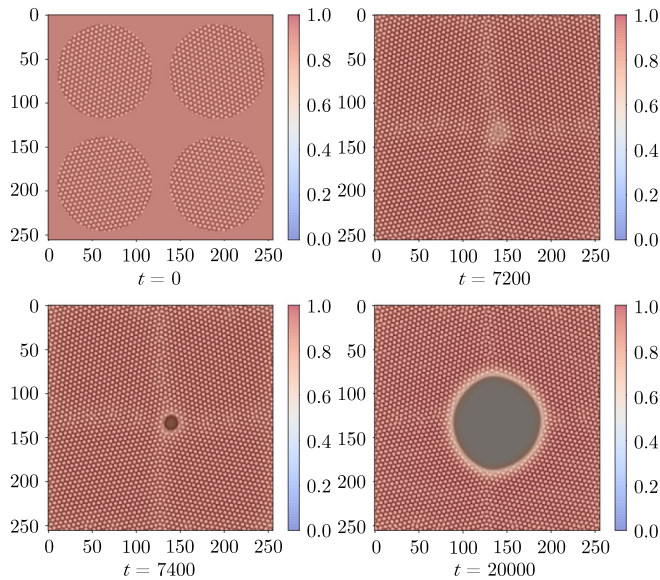


FIG. 11. Simulation of two phase coexistence in a domain of 256×256 grid points. The color scale denotes concentration, while the dark gray denotes the vapor phase. A set of four circular seeds of differing grain orientations are initiated into an underdense liquid. The solid seeds grow and coalesce, generating an artificially high energy point at which the four grains meet. This leads to the nucleation of a vapor pocket at this high-energy point, shown by the dark color. The vapor pocket grows until it reaches a stable configuration of solid-vapor coexistence. See Appendix for model description and parameters.

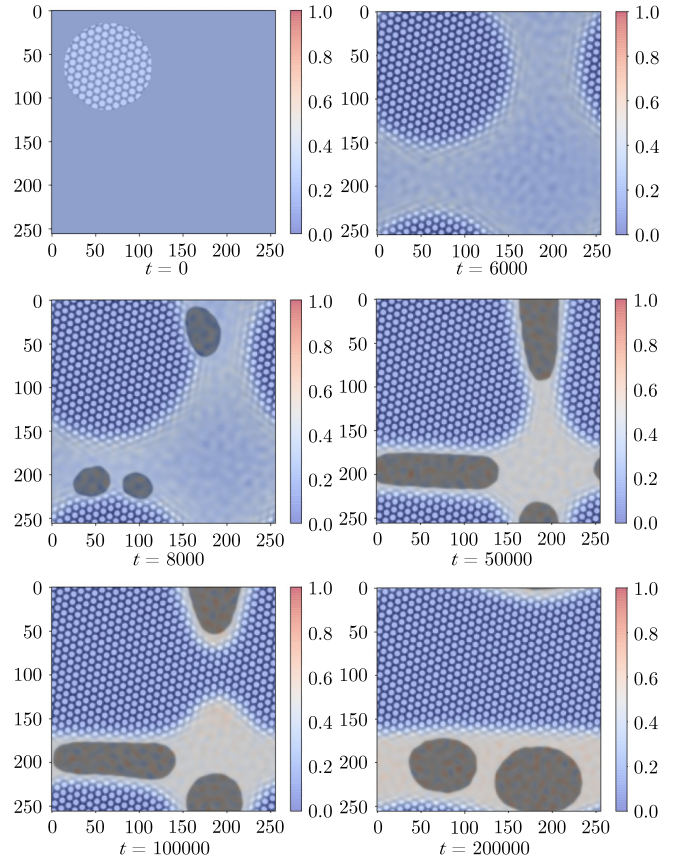


FIG. 12. Simulation within the eutectic triangle of the phase diagram of Fig. 9(a). A solid seed is initiated into an underdense liquid. The vapor phase nucleates in the depletion layer of the growing solid seed. Coarsening occurs; however, the third, solid, phase does not nucleate up to the time of this simulation due to the relatively large nucleation barrier relative to the system noise. See Appendix for model description and parameters.

any need to explicitly define concentration by smoothing the microscopic density field n . We also note that with this formulation it is numerically convenient, for simplicity, to replace $W_n |\nabla n_0|^2 + W_c |\nabla c|^2 \rightarrow W_A |\nabla n_A^0|^2 + W_B |\nabla n_B^0|^2$ such that the gradient penalty terms do not need to pass through the chain rule in the dynamics. This change is reflected in the model summary in the Appendix.

We conducted dynamical numerous simulations using Eq. (31) applied to the free energy of Eq. (30) to test the stability, growth, and coexistence of multiple alloy phases possible in the eutectic alloy system of model Eq. (30). This was done to demonstrate the robustness of our new formalism but also to test that solid phase dynamics are free of the interfacial artifacts reported in Sec. II. Moreover, we also tested our model to confirm that spinodal decomposition dynamics are free of the intermediate-time anomaly reported in Sec. II, which are also manifested in alloys that define c through a smoothing operation on the component densities.

Two typical examples illustrating the dynamics of our model are shown in Figs. 11 and 12 for quenches at the locations in the phase diagram of Fig. 9(a) marked by stars. In all cases, the domains were square with 256×256 grid points,

TABLE I. Summary of models referenced in the text and the parameters used to produce the phase diagrams and simulations in this manuscript.

| Model | Parameters | Figures |
|---|--|------------|
| $\frac{\Delta F}{\rho_0 k_B T_0} = \tau \int d^3 r \left[b_1 n_{mf} + \sum_{i=1}^9 b_i (n+1) n_{mf}^i + b_{10} n_{mf}^{10} \right]$ $- \frac{1}{2} \int d^3 r \left[n C_2 * n + \sum_{j=2}^4 \frac{a_j}{j} (n^j - n n_{mf}^{j-1}) \right]$ $C_2 = \begin{cases} \tau B_x e^{-\tau} e^{-(k-q_0)^2/(2\alpha^2)} - \tau d e^{-k^2/(2\beta^2)} & k \leq q_0 \\ \tau B_x e^{-\tau} - \frac{1}{2} \frac{\tau B_x e^{-\tau} (k-q_0)^2}{\alpha^2} & k > q_0 \end{cases}$ | $a = 4.65$ $b = 0.5$ $b_1 = \frac{\tau}{b-1} - a$ $b_{j>1} = (-1)^{1+j} + \frac{(-b)^j}{j}$ $a_2 = 2 + 6\tau + 0.17\tau^2$ $a_3 = -1.2 - 0.6\tau + 0.14\tau^2$ $a_4 = 0.11$ $q_0 = 1.0$ $\alpha = 0.1$ $\beta = 0.35$ $B_x = 1.5$ $d = 1.5$ $\lambda_c = 0.34$ | Figs. 1, 2 |
| $\frac{\Delta F}{\rho_0 k_B T_0} = \int_V dr \left\{ -\frac{1}{2} n [\tau + B_x (1 - \nabla^2)^2] n - \frac{n^3}{6} + \frac{n^4}{12} \right.$ $\left. + \frac{1}{3} (a\tau + b) n n_{mf}^2 + c n n_{mf}^3 \right\}$ | $B_x = 0.3$ $a = 35$ $b = -12.01$ $c = 33.5$ $\lambda_c = 0.21$ | Figs. 3, 4 |
| $\frac{\Delta F}{\rho_0 k_B T_0} = \int_V dr \left\{ -\frac{1}{2} (\tau + B_x) n_0^2 + \left[-\frac{1}{6} + (a\tau + b) \right] n_0^3 \right.$ $+ \left(\frac{1}{12} + \frac{c}{4} \right) n_0^4 + W_n \nabla n_0 ^2$ $+ \frac{a_2}{2} \phi^2 - \frac{a_3}{6} \phi^3 + \frac{a_4}{12} \phi^4 - \frac{1}{2} \phi C_{\phi\phi} * \phi$ $- \frac{a_3}{2} (\chi * n_0) \phi^2 + \frac{a_4}{2} (\chi * n_0)^2 \phi^2 + \frac{a_4}{3} (\chi * n_0) \phi^3 \left. \right\}$ $C_{\phi\phi} = \begin{cases} -10 + (10 + B_x) e^{-\tau} e^{-\frac{(k-1)^2}{2(10+B_x)0.5^2}} & k \leq q_0 \\ B_x e^{-\tau} e^{-(k-1)^2/(2 \times 0.5^2)} & k > q_0 \end{cases}$ | $B_x = 0.3$ $a = 35$ $b = -12.01$ $c = 33.5$ $a_2 = 1$ $a_3 = 1$ $a_4 = 1$ $W_n = 2.0$ | Figs. 4–6 |
| $\frac{\Delta F}{\rho_0 k_B T_0} = \tau \int_V dr \left\{ \frac{n_0^2}{2} - \frac{n_0^3}{6} + \frac{n_0^4}{12} + \frac{a}{\sqrt{\tau^2 + \tau_*^2}} e^{-(n_0 - n_c)^2} + W_n \nabla n_0 ^2 \right.$ $+ \frac{a_2}{2} \phi^2 - \frac{a_3}{6} \phi^3 + \frac{a_4}{12} \phi^4 - \frac{1}{2} \phi C_{\phi\phi} * \phi$ $\left. - \frac{a_3}{2} (\chi * n_0) \phi^2 + \frac{a_4}{2} (\chi * n_0)^2 \phi^2 + \frac{a_4}{3} (\chi * n_0) \phi^3 \right\}$ | $B_x = 1.3$ $a = 0.5$ $n_c = 0.0$ $\tau_* = \sqrt{0.2}$ $a_2 = 2$ $a_3 = 1.2$ $a_4 = \frac{24}{81}$ $W_n = 2.0$ $C_{\phi\phi} = C_{\text{ref}}(1.0, 0.25, 0.35)$ | Figs. 7, 8 |
| $\frac{\Delta F}{\rho_0 k_B T_0} = \tau \int_V dr \left\{ \frac{n_0^2}{2} - \frac{n_0^3}{6} + \frac{n_0^4}{12} + W_A \nabla n_0^A ^2 + W_B \nabla n_0^B ^2 \right.$ $+ \frac{(1-c)^2 a_{AA} + 2c(1-c)a_{AB} + c^2 a_{BB}}{\sqrt{\tau^2 + \tau_*^2}} e^{-(n_0 - n_c)^2}$ $+ w(n_0 + 1) \left(c \ln \left(\frac{c}{c_0} \right) + (1-c) \ln \left(\frac{1-c}{1-c_0} \right) \right)$ $+ \frac{a_2}{2} \phi^2 - \frac{a_3}{6} \phi^3 + \frac{a_4}{12} \phi^4 - \frac{1}{2} \phi C_{\phi\phi} * \phi$ $\left. - \frac{a_3}{2} (\chi * n_0) \phi^2 + \frac{a_4}{2} (\chi * n_0)^2 \phi^2 + \frac{a_4}{3} (\chi * n_0) \phi^3 \right\}$ | $W_A = W_B = 3.0$ $a_{AA} = 0.5$ $a_{AB} = 0.4$ $a_{BB} = 0.5$ $n_c = 0.0$ $\tau_* = \sqrt{0.2}$ $a_2 = 2.0$ $a_3 = 1.2$ $a_4 = \frac{24}{81}$ $w = 0.1$ $c_0 = 0.5$ $C_{\phi\phi} = X_A C_{AA} + X_B C_{BB}$ $X_A = 1 - 3(\chi * c)^2 + 2(\chi * c)^3$ $X_B = 3(\chi * c)^2 - 2(\chi * c)^3$ $C_{AA} = C_{\text{ref}}(1.0, 0.2, 0.35)$ $C_{BB} = C_{\text{ref}}(1.4, 0.2, 0.35)$ | Figs. 9–12 |

and the dimensionless time step used in each simulation was $\Delta t = 1$ (although any similar of this order is expected to give convergent results). Data for plotting was output at every 200 time steps. As discussed in the previous section on pure material simulations, the simulations using the alloy formalism introduced in this work are preformed using the semi-implicit Fourier method.

Figure 11 shows four solid seeds solidifying into a metastable liquid in the region of the phase diagram corresponding to two-phase coexistence between a single low concentration solid phase and a slightly lower concentration vapor phase. This configuration was chosen to create a high-energy grain boundary in the center of the system to lower the barrier for heterogeneous nucleation of the vapor phase, thus reducing the timescale required for nucleation.

Figure 12 is initiated with a low concentration solid seed in the region where equilibrium consists of a ternary coexistence between a low concentration α phase, a high concentration β phase and a vapor mixture. The solid phase is then allowed to grow, which prompts nucleation of the vapor phase in the depletion layer of the growing crystal. In this case we did not observe nucleation of the β phase in the timescale of the simulation. This is because the simulation is implemented with additive noise, which limits the noise amplitude that can be added to the system; due to the low densities of each component in the vapor phase, utilizing additive noise with a large amplitude can destabilize the system by generating a concentration below zero or greater than one. With this limitation on the amplitude of the additive noise, the nucleation barrier for the solid β phase becomes comparatively large and thus the timescale for nucleation becomes significantly longer.

V. CONCLUSION

This paper began by discussing a number of anomalous results than arise due to the use of filter functions in the construction of liquid-solid-vapor phase field crystal models of pure materials. To remedy this dynamical artifact, we introduced a new formalism by which the PFC density is decomposed into smooth and oscillating components, which then become the dependent fields evolved in a PFC model. The properties of each field are maintained by a careful choice of correlation functions. In addition, a phenomenology for higher-order three- and four-point correlation functions was

introduced in order to make flexible the parametrization of the free energy in each of these constituents of the density. This allowed us to model vapor-liquid-solid phase diagram both qualitatively and quantitatively. Moreover, dynamics in this new formalism are free of any anomalous features affecting the interface of solids, or domain scaling in spinodal decomposition. We generalized the new formalism to binary alloys and also demonstrate that the dynamics are also free of any of the aforementioned artifacts that emerge in previous alloy models. Our simulation examples revealed that nucleating from a vapor phase in the presence of noise with a constant amplitude can be problematic at the realistically low densities afforded by our new formalism. Further work is required to determine how to scale noise appropriately with density to make it more quantitative for low-density phases, such as vapor. This model will allow for new opportunities incorporating various void formation and cavitation processes in rapid solidification. Further, simulation of cracking is a possible application area but will likely require a second-order time derivative—such as that of Stefanovic *et al.* [8]—to capture phononic behavior. Alternatively, should an amplitude model be constructed from this model, the phononic behavior may be captured via hydrodynamics couplings as in Heinonen *et al.* [26]

ACKNOWLEDGMENTS

N.P. acknowledges the Natural Science and Engineering Research Council (NSERC) of Canada, Canada Research Chairs (CRC) Program for funding and Calcul Québec for computing resources.

APPENDIX: MODEL PARAMETERS BY FIGURE

Table I shows the various models and model parameters used to generate the figures in this manuscript. For the model of Ref. [4], we also use the notation $n_{mf} \equiv \chi * n$ for the density when it has been acted on by a smoothing kernel. For brevity we will define here the standard form of our correlation kernels,

$$C_{\text{ref}}(k; q_0, \sigma_0, \sigma_1) \equiv -10e^{-\frac{k^2}{2\sigma_0^2 q_0^2}} + B_x e^{-\tau} e^{-\frac{(k-q_0)^2}{2\sigma_1^2}}, \quad (\text{A1})$$

and unless otherwise stated, $\lambda_c = 0.2$.

-
- [1] K. R. Elder, N. Provatas, J. Berry, P. Stefanovic, and M. Grant, Phase-field crystal modeling and classical density functional theory of freezing, *Phys. Rev. B* **75**, 064107 (2007).
 - [2] K. R. Elder and M. Grant, Modeling elastic and plastic deformations in nonequilibrium processing using phase field crystals, *Phys. Rev. E* **70**, 051605 (2004).
 - [3] K. R. Elder, M. Katakowski, M. Haataja, and M. Grant, Modeling Elasticity in Crystal Growth, *Phys. Rev. Lett.* **88**, 245701 (2002).
 - [4] G. Kocher and N. Provatas, New Density Functional Approach for Solid-Liquid-Vapor Transitions in Pure Materials, *Phys. Rev. Lett.* **114**, 155501 (2015).
 - [5] G. Kocher and N. Provatas, Thermodynamic coupling in phase-field-crystal-type models for the study of rapid crystallization, *Phys. Rev. Mater.* **3**, 053804 (2019).
 - [6] Z.-L. Wang, Z. Liu, Z.-F. Huang, and W. Duan, Minimal phase-field crystal modeling of vapor-liquid-solid coexistence and transitions, *Phys. Rev. Mater.* **4**, 103802 (2020).
 - [7] N. Wang, N. Smith, and N. Provatas, Investigating gas-phase defect formation in late-stage solidification using a novel phase-field crystal alloy model, *Phys. Rev. Mater.* **1**, 043405 (2017).
 - [8] P. Stefanovic, M. Haataja, and N. Provatas, Phase-Field Crystals with Elastic Interactions, *Phys. Rev. Lett.* **96**, 225504 (2006).

- [9] M. Greenwood, N. Ofori-Opoku, J. Rottler, and N. Provatas, Modeling structural transformations in binary alloys with phase field crystals, *Phys. Rev. B* **84**, 064104 (2011).
- [10] V. Fallah, J. Stolle, N. Ofori-Opoku, S. Esmacili, and N. Provatas, Phase-field crystal modeling of early stage clustering and precipitation in metal alloys, *Phys. Rev. B* **86**, 134112 (2012).
- [11] G.-M. Lu, Y.-L. Lu, T.-T. Hu, and Z. Chen, Phase field crystal study on the phase boundary migration induced by the kirkendall effect, *Comput. Mater. Sci.* **106**, 170 (2015).
- [12] M. J. Frick, N. Ofori-Opoku, and N. Provatas, Incorporating density jumps and species-conserving dynamics in XPFC binary alloys, *Phys. Rev. Mater.* **4**, 083404 (2020).
- [13] M. E. Povarnitsyn, T. E. Itina, P. R. Levashov, and K. V. Khishchenko, Mechanisms of nanoparticle formation by ultra-short laser ablation of metals in liquid environment, *Phys. Chem. Chem. Phys.* **15**, 3108 (2013).
- [14] E. Wilson, Benchmarking a unified phase field crystal theory of multi-phase transformations, Masters thesis, McGill University, Montreal, 2021.
- [15] Z.-F. Huang, K. R. Elder, and N. Provatas, Phase-field-crystal dynamics for binary systems: Derivation from dynamical density-functional theory, amplitude equation formalism, and applications to alloy heterostructures, *Phys. Rev. E* **82**, 021605 (2010).
- [16] M. Greenwood, J. Rottler, and N. Provatas, Phase-field-crystal methodology for modeling of structural transformations, *Phys. Rev. E* **83**, 031601 (2011).
- [17] Previous PFC-amplitude papers [15,20,21] showed that the smooth field n_0 could develop large oscillation on the scale of the lattice constant due to the presence of remnant gradients that operate on n_0 even after course graining. We do not have such effects here.
- [18] N. Provatas and K. Elder, *Phase-field Methods in Materials Science and Engineering* (John Wiley & Sons, New York, 2011).
- [19] N. Goldenfeld, B. P. Athreya, and J. A. Dantzig, Renormalization group approach to multiscale simulation of polycrystalline materials using the phase field crystal model, *Phys. Rev. E* **72**, 020601(R) (2005).
- [20] D.-H. Yeon, Z.-F. Huang, K. Elder, and K. Thornton, Density-amplitude formulation of the phase-field crystal model for two-phase coexistence in two and three dimensions, *Philos. Mag.* **90**, 237 (2010).
- [21] N. Ofori-Opoku, J. Stolle, Z.-F. Huang, and N. Provatas, Complex order parameter phase-field models derived from structural phase field crystal models, *Phys. Rev. B* **88**, 104106 (2013).
- [22] N. Smith and N. Provatas, Generalization of the binary structural phase field crystal model, *Phys. Rev. Mater.* **1**, 053407 (2017).
- [23] A fully local term could also be kept as a modifier to enthalpy of mixing; for simplicity we neglect this term in this manuscript.
- [24] M. Gorenstein, A. Kostyuk, and Y. D. Krivenko, Van der waals excluded-volume model of multicomponent hadron gas, *J. Phys. G: Nucl. Part. Phys.* **25**, L75 (1999).
- [25] B. A. Jugdutt, N. Ofori-Opoku, and N. Provatas, Calculating the role of composition in the anisotropy of solid-liquid interface energy using phase-field-crystal theory, *Phys. Rev. E* **92**, 042405 (2015).
- [26] V. Heinonen, C. V. Achim, J. M. Kosterlitz, S. C. Ying, J. Lowengrub, and T. Ala-Nissila, Consistent Hydrodynamics for Phase Field Crystals, *Phys. Rev. Lett.* **116**, 024303 (2016).